THE AMERICAN SOCIETY OF MECHANICAL ENGINEERS
345 E. 47th St., New York, N.Y. 10017

93-GT-300

CALIBRATING ULTRASONIC IMAGES FOR THE NDE OF STRUCTURAL MATERIALS

Robert S. Gilmore
GE Corporate R&D
Schenectady, New York

Andreas M. Glaeser
University of California
Berkeley, California

Janet C. Wade
Garrett APD
Phoenix, Arizona

ABSTRACT

Ultrasonic imaging is taking a larger and larger role in the NDE of turbine engine materials and in support of fracture mechanics calculations. It is also playing an increasing role in quality and process control. For most fracture toughness calculations, it is necessary to establish the accuracy with which a flaw's size and shape are imaged, whether single or multiple flaws are involved, and the spacing of multiple flaws. Because of these requirements, resolution has become an issue as well as detection sensitivity. There are a number of resolution targets that can provide this type of calibration information for an ultrasonic imaging system. A fused quartz USAF 1951 target, similar to the patterns used in this work, was first used by Gilmore (1986), but Gilmore's pattern was superficial and subsurface evaluations were limited to focusing on the pattern from the opposite side of the blank and monitoring the reflection from what is now the target backwall. Work by Peyton (1977) did produce buried targets in titanium samples, but there was no practical method to produce buried targets in high-temperature ceramics until the techniques developed by Rodel and Glaeser (1987) were used to produce the targets described in this paper.

Optically transparent resolution targets make it feasible to visually verify that the resolution target has been correctly fabricated. An image of the target with a candidate ultrasonic transducer then permits quantitative image resolution estimates to be made even when the interrogating acoustic beam contains significant refractive aberration. This is important because useful subsurface images can be acquired with the use of acoustic beams that are aberrated to the point that diffraction-limited beamwidth calculations are meaningless.

This work also demonstrates how the interdisciplinary skills of manufacturing companies can be combined with those of universities to produce results that any one of the individual members of the team could not have produced alone, without significant increases in labor, time, and cost.

INTRODUCTION AND HISTORICAL REVIEW

The resolution target work was initiated to meet a specific need. In 1989 an extensive testing and evaluation project on silicon nitride as an engine structural ceramic was initiated by the Department of Energy through the Oak Ridge National Laboratory.

Allied Signal's Garrett Auxiliary Power Division was chosen as prime contractor by Oak Ridge. In order to solve the ultrasonic imaging problems posed by the necessity to detect and characterize very small flaws in silicon nitride test samples, a team was assembled that included the above authors. The calibration concept, proposed by this team, was straightforward. A USAF 1951 image resolution target (Figure 1) was to be imbedded in a transparent material that had the same ultrasonic velocity as the Norton NT-154 silicon nitride ceramic used for the bulk of the testing program. The smallest resolvable line-space combination would then define the resolution.

Military Standard 150-A describes this basic pattern, which has become known as the USAF-1951 or simply the "Air Force" target. Each element consists of two patterns oriented at right angles to each other, each containing three lines and two spaces. The line and spacing width are equal; the line length is equal to five times the line width. The change in pattern size is based on the sixth root of two; i.e., for every six target elements the number of line spaces per millimeter doubles. Each six target element set is known as a group, and the group number (0, 1, 2, 3, and 4 for the targets used in this paper) is the power of two to which the first element in the group is raised to express the number of lines per millimeter. Therefore, the numbers 0 to 4 for these targets correspond to 1, 2, 4, 8, and 16 lines per millimeter as shown in the table in Figure 1.

Targets were fabricated from transparent materials with acoustic longitudinal and shear velocities similar to those of the optically opaque NT-154. This assured that the refractive aberration (as shown in Figure 2) affecting the acoustic beam in the target would be similar to that produced in NT-154. The longitudinal (C_L) and shear (C_S) velocities in the C-axis direction in single-crystal sapphire (C_L = 11.22 mm/μsec, C_S = 6.10 mm/μsec) closely match the velocities in NT-154 (C_L = 11.15 mm/μsec, C_S = 6.16 mm/μsec).

Widespread interest in these resolution targets by other ultrasonic groups suggests that this is an effective strategy. This paper discusses work that has continued beyond the effort to develop the structural ceramic standards. The Rodel and Glaeser diffusion bonding techniques have also been used to produce buried 1951 USAF resolution

Presented at the International Gas Turbine and Aeroengine Congress and Exposition
Cincinnati, Ohio May 24–27, 1993
This paper has been accepted for publication in the Transactions of the ASME
Discussion of it will be accepted at ASME Headquarters until September 30,1993

Number of lines per millimeter in USAF resolving power test target 1951

Element No.	Group Number									
	-2	-1	0	1	2	3	4	5	6	7
1	0.250	0.500	1.00	2.00	4.00	8.0	16.0	32.0	64.0	128.
2	.280	.561	1.12	2.24	4.49	8.98	17.95	36.0	71.8	144.
3	.315	.630	1.26	2.52	5.04	10.1	20.16	40.3	80.6	161.
4	.353	.707	1.41	2.83	5.66	11.3	22.62	45.3	90.5	181
5	.397	.793	1.59	3.17	6.35	12.7	25.39	50.8	102.	203.
6	.445	.891	1.78	3.56	7.13	14.3	28.51	57.0	114.	228.

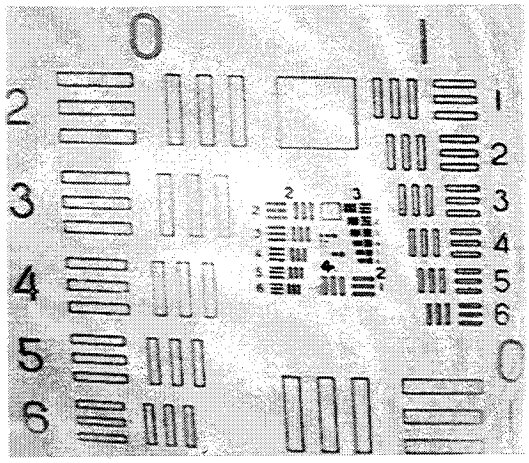

Image format – 1/4 to 228 lines/mm target

Figure 1. Table of sizes and image format for USAF resolving power test target 1951 as provided by Teledyne-Gurley Inc. Troy, NY.

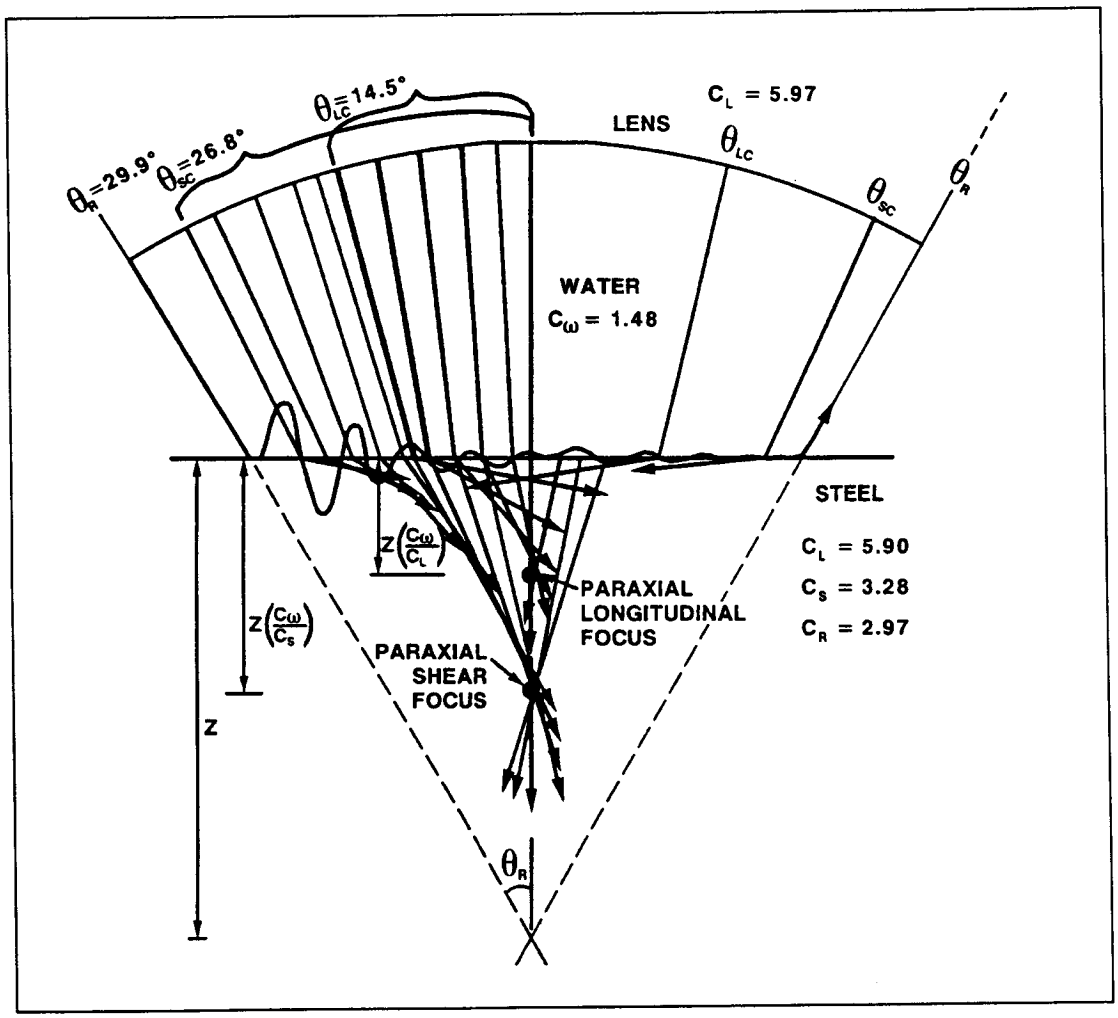

Figure 2. The angular spectrum for a water-steel interface showing the critical θ_i angles for the longitudinal (θ_{LC}), shear (θ_{SC}), and Rayleigh (θ_R) wave, and the refractive aberration caused by incidence to the water-steel interface at angles approaching $\theta_i = \theta_{LC}$, and $\theta = \theta_{SC}$.

targets in lead borosilicate glass and in [100] cut silicon. These additional target materials permit the velocities in a number of test materials to be matched to the velocity in the resolution standard. In addition to silicon nitride, sapphire can also be used to match other structural ceramics such as polycrystalline Al_2O_3, BeO, MgO, and SiC. Lead borosilicate glass produces targets that match the zirconium alloys and other lower velocity materials. The [100] cut silicon wafer sample was prepared to provide a standard to evaluate heat sink bonding integrity in silicon chip carriers for integrated circuit applications. The fused quartz resolution target used by Gilmore (1986) is a good velocity match to most structural steels, including those used for high-temperature turbine engine disks and blades. Fused quartz also is a good velocity match to the oxide loaded glasses used in computer chip carrier applications.

ULTRASONIC C-SCAN IMAGING

Mechanically scanned ultrasonic images were first used for NDE in 1954 (Buchanan and Hastings, 1955). Since then it has been further developed by Lemmons and Quate (1973), Tsai et al. (1977) and by many others (some listed in 1985), for materials characterization and evaluation, and for manufacturing process and quality control. In addition to providing a visual estimate of bond integrity, material integrity, and flaw size, the spatial correlation of the ultrasonic echoes from a flaw provides a higher probability of detection (PoD). PoD is improved, first, because the multiple echoes are spatially correlated and identified, by the imaging process, to come from single or multiple discontinuities. In addition, the signal-to-noise ratio is improved when signals scattered by the material microstructure (N) add algebraically to the flaw discontinuity signals (S) producing a (S+N)/N = S/N + 1 ratio in the image.

Ultrasonic images generally fall into one of two categories: surface images or volume images. The type of image is determined by how the incident beam is focused and how the signals are gated. These are in turn established by the transducer lens and the velocities in the material being imaged. The key considerations are summarized in Figures 3 and 4.

By restricting this discussion to quasi-isotropic materials, the acoustic properties of the material can be described by the density and three velocities. These are the longitudinal (C_L), the shear (C_S), and the surface or Rayleigh (C_R) velocities, respectively. For the materials listed in Table 1, the ratio C_L/C_S is typically about 1.6, and the ratio C_R/C_S is typically about 0.92. When an acoustic ray is incident through a fluid with a velocity C_2 onto a multiple velocity substrate with two or more refracted velocities C_L, C_S, and C_R, then the direction of the refracted rays shown in Figure 2 is described by Snell's law

$$\sin\theta(L,S,R) = \frac{C(L,S,R)}{C_i}\sin\theta i$$

where θi is the angle of the incident ray in the fluid and $\theta(L,S,R)$ are the angles of the refracted longitudinal, shear and surface rays. The values for which $\sin\theta(L,S,R) = 1.0$ are called the critical angles for each of the respective velocities. Neglecting the occurrence of nonpropagating waves and their behavior, for C_L and C_S, the critical angles of incidence are those at which longitudinal, shear, and surface waves are refracted parallel to the entry surface. For the longitudinal and shear modes, the fluid-solid interface dramatically increases in reflectance as the critical angle is approached, and since neither the longitudinal nor shear modes develop surface propagating waves, the ability of those modes of propagation to interact with the substrate material is limited by their critical angles. In comparison, the Rayleigh critical angle θ_R is the angle at which a propagating surface wave mode is generated. When the acoustic rays are considered at monotonically increasing angles of incidence (such as for the water-steel interface shown in Figure 2), a plot of the acoustic amplitudes, modes of propagation, and critical angles for the modes is often called the angular acoustic spectrum of that substrate material. Therefore, when the cone of focus is made large enough to include the Rayleigh critical angle (so that surface wave images can be made), reflections from discontinuities in the vicinity of the longitudinal and shear subsurface foci can also contribute to the image by interacting with the surface wave.

This discussion will not redevelop the beam diameter calculations summarized for surface wave imaging in Figure 3 and for volumetric

Table 1. Longitudinal, shear and surface wave velocities of selected materials and the respective critical angles. The C-Axis sapphire is reported as if it was transversely isotropic for the shear and surface wave velocities. This is only approximate.

Material	Density	C_L mm/μsec	C_S mm/μsec	C_R mm/μsec	θ_L (degrees)	θ_S (degrees)	θ_R (degrees)
H_2O (22°C)	1.0	1.48					
[001] sapphire	3.99	11.22	6.10	5.50	7.6	14.0	15.5
[100] silicon	2.33	8.90			9.6		
[111] silicon	2.33	9.37			9.1		
NT-154 SiN	3.25	11.15	6.16	5.54	7.6	13.9	15.5
SiC (HIP'ed)	3.25	12.65	6.25	5.92	6.7	13.7	14.5
Fused SiO_2	2.22	5.97	3.74	3.44	14.2	23.3	25.5
Sintered Diamond	3.87	16.49	11.20	9.89	5.2	7.6	8.6
Steel	7.9	5.90	3.28	2.97	14.4	26.8	29.9
Inconel 718	8.3	6.10	3.18	2.95	14.0	27.7	30.1
Lead Glass	3.65	4.21	3.12	2.90	20.5	28.3	30.7
Zirconium	6.49	4.80	2.40	2.22	18.0	38.1	41.8

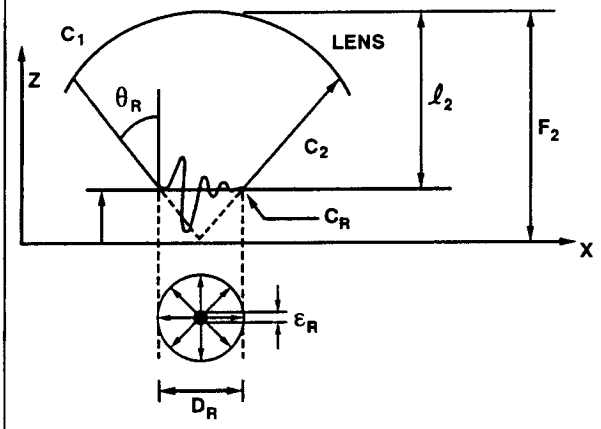

$D_R = 2Z \tan \theta_R$

$= 2[F_2 - \ell_2] \tan \theta_R$

λ_R = SW WAVELENGTH

C_R = SW VELOCITY

$\varepsilon_R\big|_{-3dB} = 0.32\ \lambda_R$

$\varepsilon_R\big|_{-1dB} = 0.16\ \lambda_R$

$\varepsilon_{RZ}\big|_{-3dB} = \lambda_R$ (BROADBAND PULSES ONLY)

D_R = Diameter of entry circle produced by the intersection of the Rayleigh critical angle cone with the entry surface.

λ_R = Wavelength of the Rayleigh wave on the entry surface.

C_R = Velocity of the Rayleigh wave on the entry surface.

ε_R = -3 dB diameter of the amplitude maximum caused by the convergence of the Rayleigh waved at the center of the Rayleigh entry circle. Defines 1 shade of gray or resolution produced by the beam convergence.

ε_R = -1dB diameter of the amplitude maximum described above. Used to specify the pixel size/spacing for the image.

ε_{RZ} = -3 dB sensitivity drop of a broadband Rayleigh wave (less than 2 wave pulse length) beneath the surface of propagation.

Figure 3. Summary of the equations and the parameters describing the diffraction limited resolution for a time resolved surface wave image.

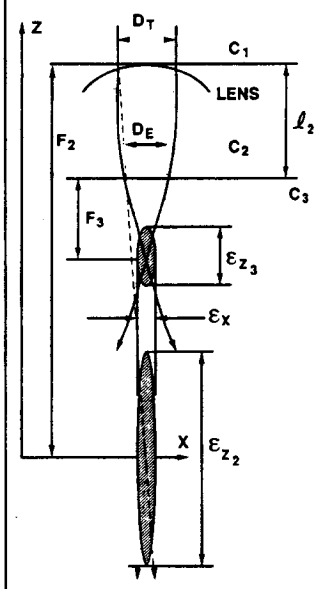

SPHERICAL FOCUS $F/D \geq \frac{C_3}{C_2}$

$\varepsilon_X\big|_{-3dB} = 1.03\ \lambda_2 \frac{F_2}{D_T} = 1.03\ \lambda_3 \frac{F_3}{D_E}$

$\varepsilon_X\big|_{-1dB} = 0.4\ \lambda_2 \frac{F_2}{D_T}$

$\varepsilon_{Z_2}\big|_{-3dB} = 4\ \lambda_2 \left[\frac{F_2}{D_T}\right]^2$

$\varepsilon_{Z_3}\big|_{-3dB} = 4\ \lambda_2 \left[\frac{F_2}{D_T}\right]^2 \frac{C_2}{C_3} = 4\ \lambda_3 \left[\frac{F_3}{D_E}\right]^2$

$F_3 = [F_2 - \ell_2] \frac{C_2}{C_3} \quad \lambda_3 = \frac{C_3}{C_2} \lambda_2$

$D_E = \frac{F_2 - \ell_2}{F_2} D_T$

$\frac{F_3}{D_E} = \frac{F_2}{D_T} \frac{C_2}{C_3}$

C = Ultrasonic velocity in the lens (C_1), the water or coupling fluid (C_2), and the part (C_3), respectively.

λ = Ultrasonic wavelengths (velocity/frequency), for the lens (1), water (2), and part (3), respectively.

F = Focal length produced by the transducer lens in the water (F_2), and part (F_3), respectively.

D_T = Diameter of the transducer element and/or lens.

D_E = Diameter of ultrasonic beam on entry into the part.

ε_X = -6 dB and/or -1 dB beam diameters of diffraction limiter focal zones in either the water or the part. -6 dB is industry standard for transducer characterization, - 1dB is used to determine pixel size for imaging.

ε_Z = -3 dB depths of the focal zones produced by the transducer lens in the water (ε_{Z_2}), and part (ε_{Z_3}).

l = Transducer lens to part distance (water path).

X = Coordinate axis perpendicular to acoustic axis.

Z = Coordinate axis parallel to acoustic axis.

Figure 4. Summary of the equations and the parameters for the lateral resolution produced by a diffraction limited focused acoustic beam in a beam forming fluid or in a high-velocity substrate.

imaging in Figure 4. Similar calculations have been well discussed by Liang et al. (1985), by Gilmore (1986 and 1988), and by others (1985). What this paper wishes to emphasize is that subsurface foci in high-velocity substrates almost always contain significant refractive aberration, such as shown in Figure 2. In addition, they also contain micro-aberrations due to grain-to-grain anisotropy. The use of single crystal and glass resolution standards eliminates grain anisotropy from the resolution standard images. However, grain-to-grain anisotropy is the mechanism that permits all acoustic images, and particularly surface waves, to image the microstructure. In fact, surface wave images of microstructure are simply micro-aberration images. For volumetric imaging, unless the ratio of transducer focal length to diameter in the fluid is equal to or greater than the velocity ratio of the substrate/fluid interface, (F/D C_3/C_2, Figure 4), the most straightforward method to determine the resolution produced at a subsurface plane in a high-velocity solid is to scan a resolution target fabricated from the subject material or a velocity-matched material.

STANDARDS FOR ULTRASONIC INSPECTION METHODS

The development of standards for establishing the sensitivity and resolution of all ultrasonic NDE inspection methods has proven to be an ongoing problem for the testing industry. The traditional sensitivity standard is a flat bottomed hole (FBH), first proposed by the Krautkramers (1959). Drilled into materials that are identical in composition and in microstructure to those being inspected, the FBH provides a reflector of known circular (and therefore mathematically definable) scattering cross section. Since, as a first-order approximation, pulse-echo amplitude is linearly proportional to the area of a compact flat reflecting void perpendicular to the acoustic axis of the interrogating beam, the FBH area establishes the reflecting area that can be detected, hence the test sensitivity. However, an ultrasonic image of a single hole can only show that it was detected; no resolution information is supplied. Another drawback is that the circular bottom of the hole is always accompanied by a cylindrical shaft connecting it to the drilled surface, and therefore it is surface connected and only approximates the buried circular void/crack it is intended to represent. In addition, for materials with scattering microstructures (i.e., materials with grains, or more than one material such as composites) the echoes from the bottoms of small holes add algebraically to the grain boundary reflections, producing significant echo amplitude variations from holes of precisely the same size. Therefore, single reflector calibration blocks can over-calibrate or under-calibrate depending on the location of the FBH in the material microstructure. In order to meet these problems and to solve the sensitivity/resolution dilemma, standards have been developed with multiple hole patterns (Mitchell and Gilmore, 1992, Figure 5). These hole patterns can determine the variance in amplitude and resolution produced by scattering materials and are easy to make for materials that can be drilled, such as titanium, steel, and zirconium. But ceramics are difficult to drill, and holes only a few microns in diameter, such as are required to calibrate inspections for small voids in structural ceramics, are especially difficult.

DEVELOPMENT OF IMAGING STANDARDS WITH PHOTOLITHOGRAPHY

Lithography has furnished a new tool for studying and for creating subsurface void arrays with very precise geometries. These arrays may be produced in high temperature structural ceramics, in many glasses, and at ceramic-metal interfaces. The combination of photolithographic

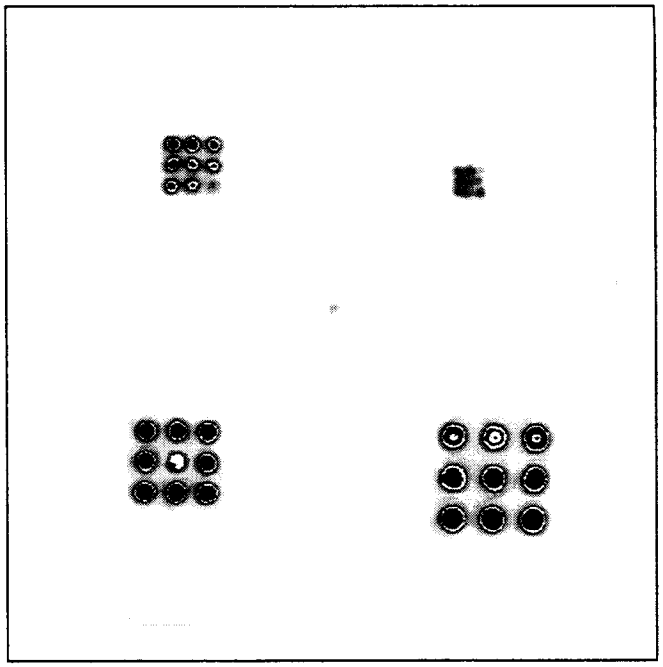

Figure 5. Acoustic image of a block with multiple flat bottomed holes. There are four 3×3 arrays of holes spaced at the hole diameter, and a single hole at the block center. Each array has nine holes with diameters of 400, 800, 1200, and 1600 microns, respectively. The single hole is 400 microns. Note that the 400 micron holes are detected but not resolved (separated) by the 20 MHz, F/7.0 acoustic beam, which is 500 microns in diameter.

methods with ion beam etching and hot pressing provides the ability to first produce surface features with highly precise geometries and locations and then to transform these features into internal features without losing this detail. The methods summarized here are reported in greater detail elsewhere (Rodel and Glaeser, 1987 and 1989).

The basic steps for the manufacture of subsurface target-void patterns are shown schematically in Figure 6. A flat, optically polished substrate (single-crystal or polycrystalline) is coated with a uniformly thick photoresist layer. Using typical process conditions, the photoresist layer may be from 1.3 to 2.6 μm in thickness. The photoresist is then selectively exposed to ultraviolet radiation using a mask to control the shape of the exposed features. This mask is produced by pattern generation software, and in this case the USAF resolution target (purchased from Teledyne-Gurley, Troy, NY) provided the design. For positive photoresists, exposure increases the solubility of the layer and therefore permits its selective removal, exposing the substrate. Ion beam etching is then used to etch the exposed ceramic surface and thereby transfer the pattern to the ceramic substrate. After removal of the remaining photoresist, an etched and unetched sample may be bonded to place the void pattern at an internal interface.

For the sapphire target used to produce the acoustic images in Figures 8a, 8b, and 8c, vacuum hot pressing (1370°C, 15 MPa, 2.6 milliPascals) was used to bond a 1.5-mm-thick unetched single crystal [001] sapphire slab to a 3.0-mm-thick etched slab of the same [001] orientation. This produced the USAF-1951 target embedded in a volume of single-crystal sapphire. The target contains bar-space patterns 0, 1, 2, 3, and 4, as described in Figure 1, with an entry surface to target-pattern depth of either 2.0 or 4.0 mm. Referring to the table in Figure 1, these range from 1 to 28.5 lines per millimeter. Note that in

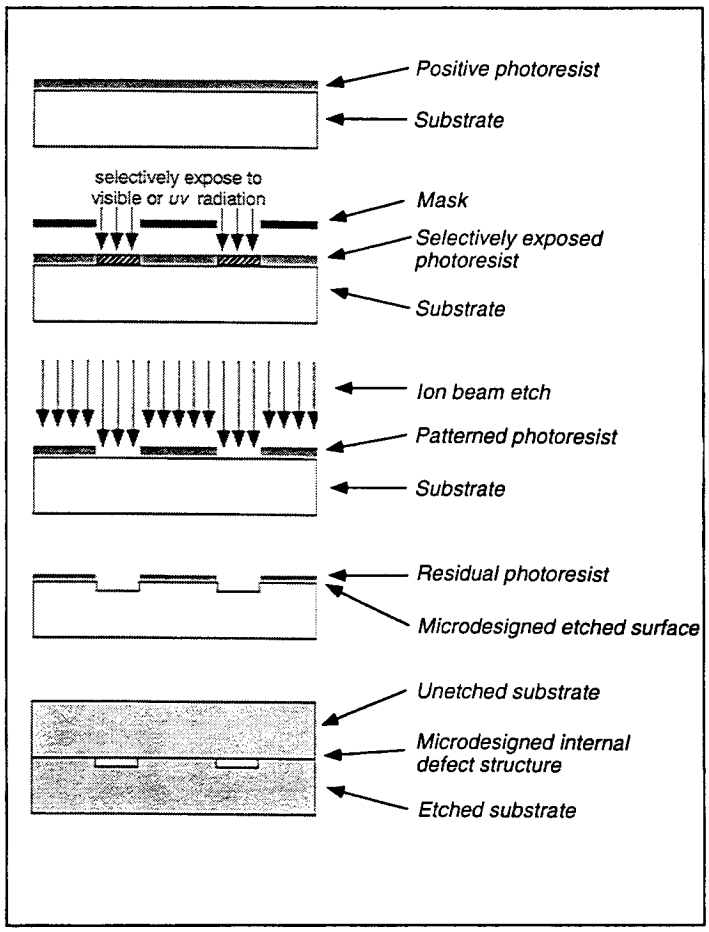

Figure 6. Schematic illustration of the procedure used to produce the subsurface target pattern in single-crystal sapphire blanks 1.5 mm and 3.0 mm thick. (a) coated substrate, (b) selective exposure through a USAF 1951 mask, (c) ion beam etching of substrate and patterned photoresist, (d) etched photoresist and sapphire, and (e) bonding of etched and unetched sapphire blanks.

addition to possessing the geometrical precision required for image calibration, these void arrays are truly buried flaws surrounded by intact solid material. They scatter sound like the subsurface cracks they are.

RESULTS

Figure 7a shows a 1024 point × 1024 point image of an area 25.4 × 25.4 mm of the USAF 1951 pattern etched into the surface of a fused quartz plate. The 50 MHz, F/0.8 acoustic beam was focused by a lens 6.37 mm in diameter and with a 4.8 mm focal length in water at ambient conditions. The resolution target (consisting of groups 0, 1, 2, 3, and 4, as discussed above) is etched into the surface of a fused quartz plate 1.5 mm thick. The image was acquired by focusing the acoustic beam directly on the patterned water-quartz interface, gating the back-reflected amplitude, and acquiring a pixel every 25 microns. Focused in this manner, the transducer produces a –6 dB diffraction limited beam that is also 25 microns in diameter.

Figure 7b is a magnified image of the same data file displaying the full resolution of that file. The 25 micron beam and pixels show good resolution for the largest bar-space patterns in Group 4 (16 lines/mm or 62.5 micron line-line spacing), but the smallest patterns in the group (almost 32 lines/mm, 31.2 micron line-line spacing) are not resolved. This observation provides one more verification of the Nyquist theorem applied to spatial resolution. Stated simply: in order to resolve dimension "d," image data must be acquired at a sampling interval less than or approaching "d/2." Applying Nyquist to the 25 micron acoustic beam used to acquire the data file for Figures 7a and 7b indicates that the micron pixels do not support the 25 micron resolution provided by the beam. In order to support the beam, the pixel size/spacing should be less than 12.5 microns. However this was beyond the capability of the scanner at the time this file was acquired.

Figure 7c shows the same data file undersampled by two in each direction, increasing the pixel size to 50 microns. Note that it is now not possible to resolve even the largest pattern in Group 4 of the resolution target. However, looking at the next largest group, it can be observed that the patterns in Group 3 (upper right in the Figure 7c image) show the same respective definition that Figure 7b displayed for Group 4. Since the spatial resolution was decreased by a factor of two the result should be expected.

Figure 8a shows a 1024 × 1024 longitudinal wave image of the 25.4 mm × 25.4 mm sapphire target described above. The 50 MHz, F/3.0 transducer used to acquire the image used a 6.37 mm diameter lens focusing the beam at 19.05 mm in water. This produces a half angle of incidence of 9.5°, well beyond the 7.6° critical angle of incidence for longitudinal waves in water incident on a C-Axis sapphire substrate (Table 1). The longitudinal focus produced in sapphire is similar to that shown for steel in Figure 2 (between 0° and 14.5°). Clearly, diffraction limiting conditions do not control the resolution in this image.

A display of the raw data as shown in Figure 8b is able to resolve only the first two patterns in Group 2 (a little better than 4.5 lines/mm or 220 microns). The resolution inherent to the high spatial frequency of the image (25 micron pixel size), however, can still be utilized. Figures 8b and 8c show a magnified view of the outlined portion of Figure 8a and then enhance the resolution using a Wiener filter image processing technique described elsewhere (Mitchell and Gilmore, 1992). Note that in Figure 8c the patterns resolved in Group 3 suggest that the processed image shows twice the resolution of the unprocessed image.

Figure 9 shows a 50 MHz, F/4.0 image of a target fabricated from lead borosilicate glass. The image was made at a surface to pattern distance of 8.06 mm. The transducer lens is 6.35 mm in diameter and focuses at a distance of 25.4 mm in water, producing an angle of incidence for the marginal rays of 7.2°. Since this is well within the 20.7° first critical angle of the material, the resolution in the image will be controlled by the –6 dB transducer beam diameter (120 microns). Applying the Nyquist criterion to the 120 micron beam diameter, i.e., doubling the beam diameter (240 microns) should indicate the approximate resolution limit in the image. Note that in Figure 9 the first four elements in Group 2 are resolved and that the largest element in Group 2 is spaced at 4.0 lines/mm (250 microns) and that elements spaced less than 5.66 lines/mm (177 microns) can not be readily resolved, (from list in Figure 1).

Figure 9 also shows, however, that in this target all the lines in Group 0, the lines in the largest element in Group 1, and all of the solid squares have had their central regions bonded by the hot pressing process. Therefore just as the target can be used to evaluate the acoustic image, the image can also be used to evaluate the target (fabrication process). A somewhat more moderate temperature/pressure combination is indicated for future targets fabricated from lead borosilicate glass.

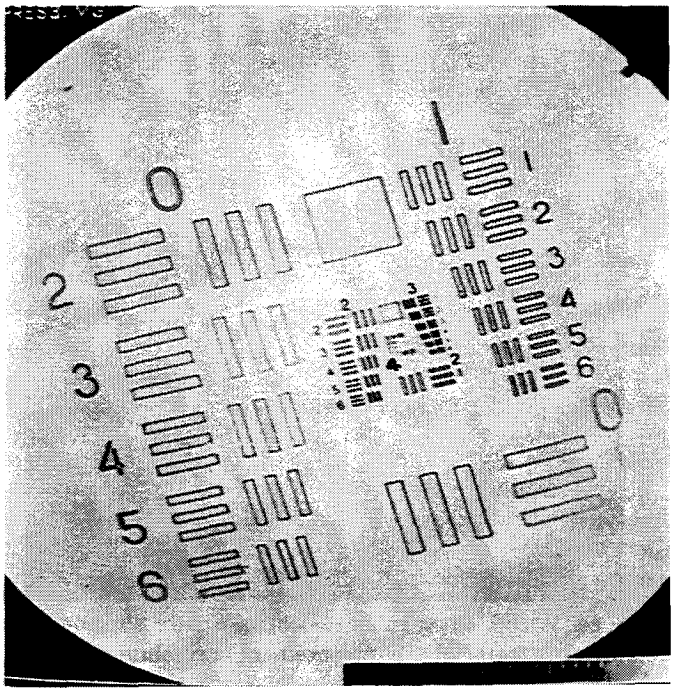

Figure 7a. 50 MHz, F/0.8 image of USAF 1951 pattern etched on the surface of a fused quartz plate. The 1024 × 1024 image covers 25.4 × 25.4 millimeters, making the pixel size 25 microns, which is also the transducer beam diameter.

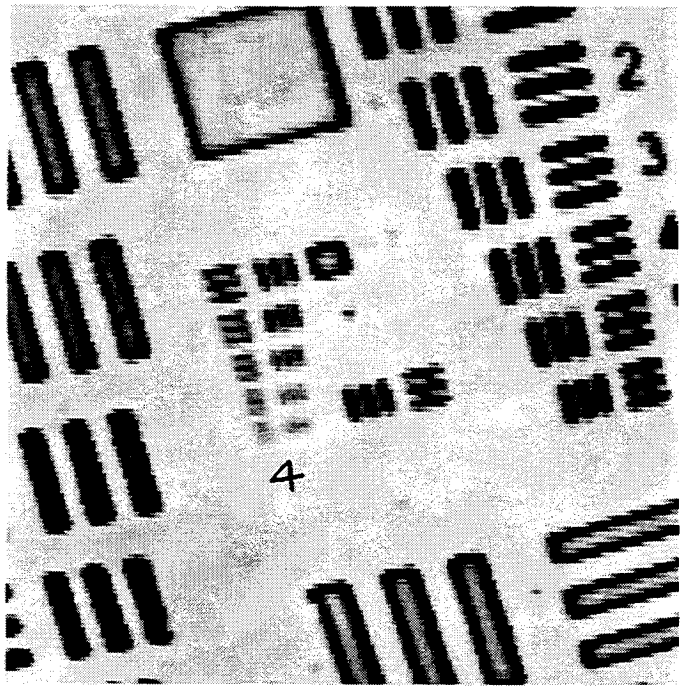

Figure 7b. Magnified image of the Group 4 segment of Figure 7a. The 25 micron pixels are now visible, as is the loss of resolution as the line pairs approach 32 lines/mm.

CONCLUSIONS

For subsurface ultrasonic imaging, high-velocity materials result in low numerical apertures for the penetrating acoustic beam and therefore low resolution for an image of an interior plane. The purpose of this discussion was to demonstrate a pragmatic method for establishing the resolution that can be achieved at depth in high-velocity substrates, even in the presence of considerable refractive aberration. The velocity range available in transparent materials (glasses, oxides, and silicates) combined with the possibilities to create buried target patterns by diffusion bonding makes it possible to develop resolution standards for most materials. Standards such as those discussed here have been of considerable use to the authors of this paper for characterizing the resolution in their ultrasonic imaging systems. As demonstrated, these targets are also of considerable use in evaluating image processing techniques.

ACKNOWLEDGMENTS

Part of the work to develop the sapphire targets was funded by DoE Contract 86X-SC674C through the Oak Ridge National Laboratory. The authors would like to thank Jeffery B. Platt and Patrick J. Howard for their assistance in the display and processing of some of the ultrasonic images used in this discussion and to Harold D. Ackler for assistance in making the targets.

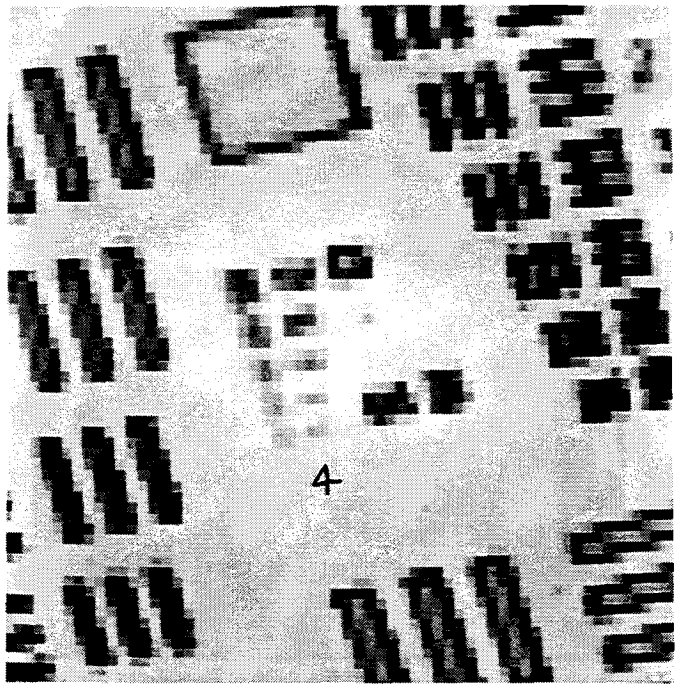

Figure 7c. Image of the same area as in Figure 7b but undersampled in two directions by a factor of two. The image now displays Group 3 patterns with the same relative resolution as in Figure 7b resolved in Group 4.

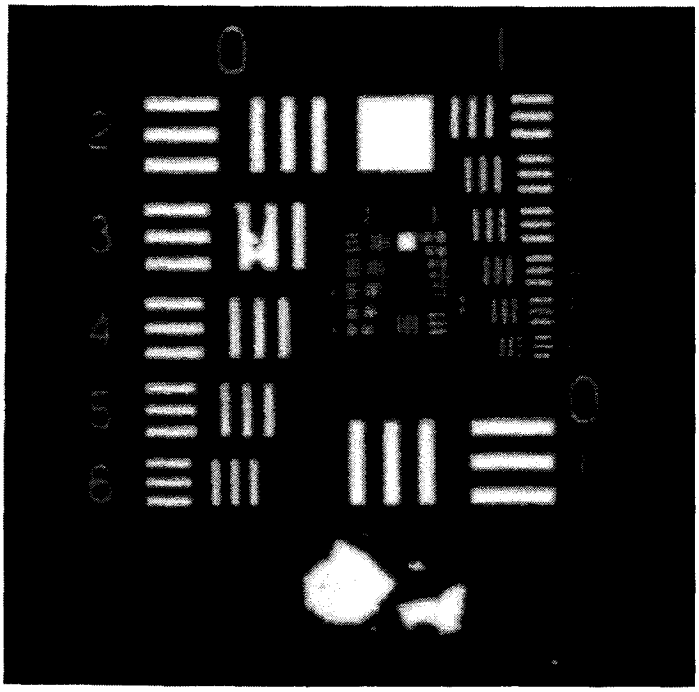

Figure 8a. 50 MHz, F/3.0 image of the sapphire resolution target taken from the 1.5 mm surface to pattern depth. The flaws evident in the image were actually very useful. One of the smallest was used to define the point-spread beam function used to provide the image enhancement shown in Figure 8c.

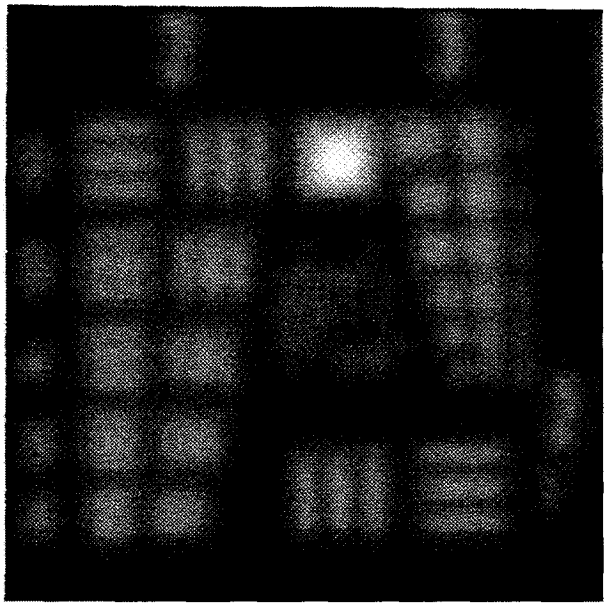

Figure 8b. Magnified image of the central portion of Figure 8a.

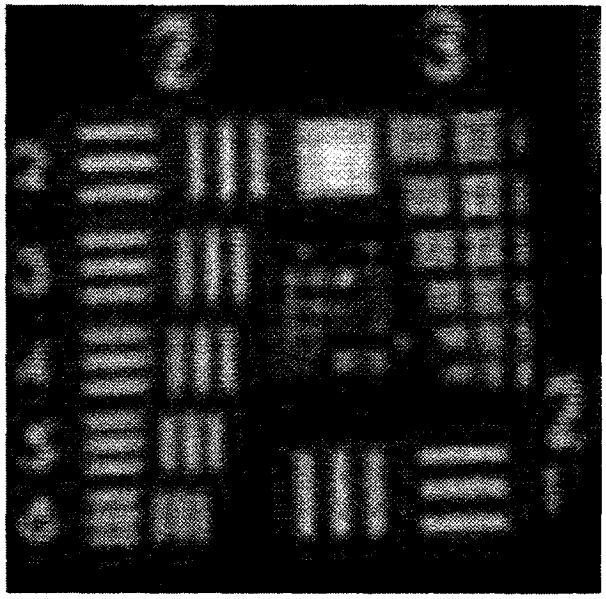

Figure 8c. Wiener filter enhancement of Figure 8b showing approximately a factor of two improvement in resolution.

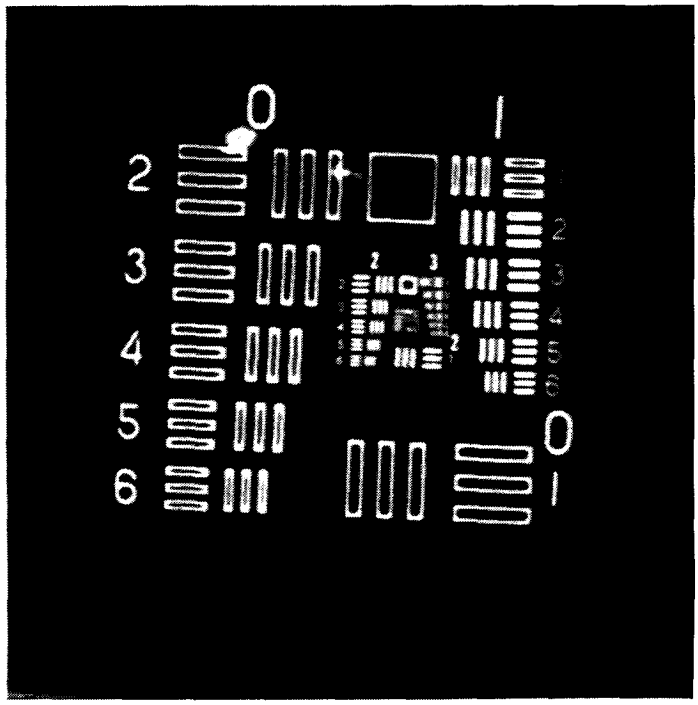

Figure 9. 50 MHz, F/4.0 image of the lead borosilicate glass target from the 8.1 mm surface to pattern distance.

REFERENCES

Buchanan, R.W., and Hastings, C.H., (1955), "Ultrasonic Flaw Plotting Equipment: A new Concept in Industrial Inspection," *Nondestructive Testing*, Volume 13, No. 5, pp. 17-25.

Gilmore, R.S., Tam, K.C., Young, J.D. and Howard, D.R., 1986, "Acoustic Microscopy From 10 to 100 MHz for Industrial Applications," *Philosophical Transactions of the Royal Society, London*, A320, pp. 215-235.

Gilmore, R.S., Hewes, R.A., Thomas III, L.J., and Young, J.D., (1989), "Broadband Acoustic Microscopy: Scanned Images with Amplitude and Velocity Information," *Proceedings of the 17th Annual Symposium on Acoustic Imaging*, Ed. by Shimizu, H., Chubachi, N., And Kushibiki, J., Volume 17, Plenum Publishing, NY, pp. 97-110.

Krautkramer, J. and Krautkramer, H., (1977), *Ultrasonic Testing of Materials*, Springer-Verlag, Berlin, FRG.

Lemons, R.A. and Quate, C.F., 1973, "Acoustic Microscopy by Mechanical Scanning," *Applied Physics Letters*, Volume 24, pp 165-167.

Liang, K.K., Kino, G.S., and Kuri-Yakub, B.T., (1985), "Material Characterization by the Inversion of V(z)" *IEEE Transactions on Sonics and Ultrasonics, Special Issue on Acoustic Microscopy*, Volume SU-32, No. 2, pp. 213-224.

Mitchell, K.W., and Gilmore, R.S., 1992 "A True Wiener Filter Implementation for Improving the Signal to Noise in Acoustic Images," *Review of Progress In Quantitative NDE*, Volume 11, Edited by D.O. Thompson and D.E. Chimenti, Plenum Press, NY.

Others (1985b), *IEEE Transactions on Sonics and Ultrasonics, Special Issue on Acoustic Microscopy,* Volume SU-32, No. 2, pp. 213-224.

Rodel, J. and Glaeser, A.M., 1989, "Photolithography: A New Tool for Ceramic Science," *Materials Research Society Symposium Proceedings*, Volume 155, pp. 293-306

Rodel, J. and Glaeser, A.M., 1987, "Production of Controlled-Morphology Pore Arrays: Implications and Opportunities," *Journal of the American Ceramic Society*, Vol. 70, No. 8, pp. c172-c176.

Tsai, C.S., Wang, S.K., and Lee, C.C., (1977), "Visualization of Solid Material Joints Using a Transmission Acoustic Microscope" *Applied Physics Letters*, Volume 31, pp. 791-793.